frontiers | Frontiers in Materials

TYPE Original Research
PUBLISHED 07 September 2023
DOI 10.3389/fmats.2023.1129818

OPEN ACCESS

EDITED BY
Jie-Sheng Chen,
Shanghai Jiao Tong University, China

REVIEWED BY
Osama A. Fouad,
Head of Nanostructured Materials and Nanotechnology Department, Egypt
Damian C. Onwudiwe,
North-West University, South Africa
Opeyemi Alice Oyewo,
Tshwane University of Technology, South Africa

*CORRESPONDENCE
Sawsan A. Mahmoud,
sawsanhassan2003@yahoo.com

RECEIVED 22 December 2022
ACCEPTED 01 August 2023
PUBLISHED 07 September 2023

CITATION
Bendary SH, Hashem AA and Mahmoud SA (2023), High efficiency dye-sensitized solar cells with a novel two dimensional Cd-V-LDH photoanode. *Front. Mater.* 10:1129818. doi: 10.3389/fmats.2023.1129818

High efficiency dye-sensitized solar cells with a novel two dimensional Cd-V-LDH photoanode

Samar H. Bendary[1], Amira A. Hashem[2] and Sawsan A. Mahmoud[1]*

[1]Egyptian Petroleum Research Institute, Nasr City, Cairo, Egypt, [2]Faculty of Women for Art, Science and Education, Ain Shams University, Heliopolis, Cairo, Egypt

The present study demonstrates a novel photoanode layer double hydroxide (LDH) for dye-sensitized solar cells (DSSCs). The search for a photoanode (PA) with low cost and high power conversion efficiency (PCE) has become one of the most significant challenges facing researchers. LDH has proven successful as a photocatalyst in various fields. In this paper, a novel Cd-V-LDH with a molar ratio of Cd:V = 1:1 was synthesized by the coprecipitation method and used as a novel PA in $DSSC_S$. X-ray diffraction (XRD), Raman spectroscopy, Scanning electron microscopy (SEM), Fourier Transform infrared spectroscopy (FTIR), Nitrogen sorption analysis, UV–Vis absorption spectrum, Electrochemical impedance spectroscopy (EIS) and cyclic voltammetry (CV) were used to examine the produced Cd-V-LDH. Cd-V-LDH as PA, Eosin Y (EY) as a photosensitizer, LiI-I_2 as a liquid electrolyte, and g-C_3N_4 (GN) as a photocathode (PC) are the component of DSSCs. The series cells of DSSCs were assembled and the available variables have been studied to achieve the best performance under normal conditions. These variables, e.g., concentration and pH of EY, active area of PA, and different types of PC, e.g., graphene oxide (GO), commercial carbon (CC), and (GN). The open circuit voltage (V_{OC}) and short circuit current density (J_{SC}) for the Cd-V-LDH/EY/LiI-I_2/GN system were observed to be 705 mV and 12.40 mA/cm^2, and has a PCE of 5.4% comparable to Cd-V-LDH/EY/LiI-I_2/GO and Cd-V-LDH/EY/LiI-I_2/CC, which have PCEs of 4.9% and 3.8%, respectively, in the identical testing conditions.

KEYWORDS

cadmium vanadium composite, dye sensitized solar cells, fill factor, conversion efficiency, layered double hydroxide

1 Introduction

Many researchers are very interested in DSSCs because of their various benefits, including their low cost, simplicity in production, and high PCE (O'regan and Grätzel, 1991; Hagfeldt et al., 2010; Grätzel, 2003; Mahmoud et al., 2017; Mahmoud et al., 2016; Mahmoud and Fouad, 2015; Mahmoud et al., 2021a). DSSCs are considered a promising alternative to silicon cells. DSSCs can meet wide photovoltaic applications not only because they are easy to manufacture but also because of recent studies revealing their superior performance when tested in indoor lighting compared to any other static PV technology (Xu and Sun, 2011). The DSSCs are assembled from multiple components, and the working anode (n-type oxide), in particular, is the primary component of visible light capture in DSSCs. Therefore, the quest for new forms of photocatalysts has become a considerable

challenge today (Mahmoud et al., 2022). LDH are promising materials for photocatalytic applications, notably in DSSCs. This is due to their high specific surface area, tuneable structure, straightforward synthesis processes, low cost, and stability. LDH also known as anionic clays or hydrotalcite like materials, has found many uses, including various applications, such as removal of environmental hazards (Mostafa and Mohamed, 2016; Abd-Ellatif et al., 2022) and DSSCs (Zhang et al., 2014; Cao et al., 2017a; Zhu et al., 2017a; Wang et al., 2020; Ge et al., 2021). The structure provides the standard anion properties of LDH that make them novel among the clay products, a large portion of which display deposits of cation properties. In the fields of lithium batteries, sensors, and catalysts, transition-metal vanadate (M-V-O) has been reported as an active material. The ternary system's valence band (VB) consists of hybridized V3d, O2p, and transition-metal orbitals (such as Bi 6s, Ag 4d, and Gd 4f), resulting in a rise in the VB level and a narrowing of the gap in the band (Zou et al., 2001; Ye et al., 2002; Kohtani et al., 2003; Sayama et al., 2003; Li et al., 2008; Zhao et al., 2008; Ke et al., 2009; Walsh et al., 2009; Mahmoud et al., 2019; Ge et al., 2021). Hence, transition-metal vanadate usually has moderate band gaps and shows great potential in the field of photocatalysis.

GN has become a prominent point in materials science for several reasons: 1) special electronic structure, 2) a medium band gap, and 3) thermal and chemical stability. Therefore, it is now among the most promising photocatalytic materials for a variety of applications (Mahmoud et al., 2021b). Graphene-based carbons, including GN and other sp2-carbon materials, receive great interest as PC in DSSCs. Further, some research has been reported proving the efficiency of carbon electrodes outperforming platinum in catalytic activity and long-term stability (Oshikiri et al., 2002).

The synthesis of LDHs still faces significant difficulties. In order to attain the best material features at low energy levels, one strategy is to employ the best formed structure possible. A second strategy is to avoid volume expansion and gas formation during prolonged circulation. Stability is reduced as a result of the active material shedding that occurs. An efficient method to uniformly grow the active material in a non-bonded *in situ* growth on the conductive current collector and improve the adhesion with the current collector to improve the electro-chemical performance is to design a large specific surface area and nanostructured material. There are several possible methods to synthesis different types of LDHs.The mixing may not be homogenous when LDHs are made via co-precipitation in a batch, which makes it difficult to replicate the quality of the final product (Shiba and Ogawa, 2018). The preparation of LDHs was done in a flow reactor to get over this limitation. Self-diffusion was used to produce quick mixing because the cross-section area of the microreactor at the mixing point is in the micrometre range.

The size, morphology, and shape of nanomaterials have a significant impact on their characteristics, which in turn are influenced by the synthetic process used (Caschera et al., 2009). LDHs can be made using a variety of methods. The chemical route, which involves bulk synthesis, is the one that is most frequently utilized, but there are alternative synthetic methods available, including electrochemical deposition. This method ensures the production of LDH films on any conductive support, including porous substrates and transparent or flexible electrodes, regardless of shape or size (Tonelli et al., 2021). The production of LDH by hydrothermal treatment of aqueous slurries at 110°C was later reported by Xu and Lu (2005). Synchrotron irradiation was used to test the hydrothermal treatment *in situ* at temperatures between 100°C and 240°C (Mitchell et al., 2007). Microwave heating has been applied to synthesize LDHs (Benito et al., 2007). The synthesis of LDHs has been carried out using ultrasonication. The wide size distribution is caused by the simultaneous development of crystals and nuclear fusion. By separating the nucleation and ageing steps using a colloid mill, Zhao et al. (2002) established a method for the manufacture of LDHs to get smaller particle size distribution (Zhao et al., 2002). The process of "mechanochemical synthesis," in which mechanical energy is employed to trigger a chemical reaction that creates material, has attracted attention (Zhang and Dai, 2017). By simply pulverising the raw ingredients using a mortar and pestle or using a mill (such as a ball mill or planetary mill), mechanical forces like compression, shear, and friction are utilized to trigger the reaction.

Several kinds of LDHs such as ZnAl-LDH (Zhu et al., 2017a; Zhu et al., 2017b), TiO_2@ZnAl-LDH (Foruzin et al., 2016), graphene/ZnAl MMO (Cao et al., 2017a; Cao et al., 2017b), graphene/ZnTi MMO (Cao et al., 2016), TiO_2@ NiAl (Foruzin et al., 2019; Andrea al., 2021), and Zn/Al LDH (Andrea et al., 2021) have been applied as working electrode in DSSCs. However, when LDHs are used as the working electrode, achieving weak power conversion performance continues to be a significant challenge.

This study focuses on the synthesis of a novel LDH material based on divalent Cd^{+2} and trivalent V^{+3} cations with a molar ratios of 1:1 by the coprecipitation method. The application of the synthesized LDH as PA, with GN as PC in DSSCs.

2 Experimental

2.1 Materials

Cadmium chloride ($CdCl_2$), Vanadium chloride (VCl_3) (Sigma-Aldrich), Sodium hydroxide (Fisher chemical), Sodium carbonate (Na_2CO_3), Triton-X100 (TX100), EY, LiI-I_2 electrolyte, and conducting glass slides from Indium doped tin oxide (ITO) (8–12 Ω/sq) (Sigma-Aldrich). All the used materials were general grade chemicals.

2.2 Synthesis of Cd-V-LDH as PA

Cd-V-LDH with Cd:V molar ratio = 1:1, was prepared by the co-precipitation method at pH 10, as shown in Figure 1. Two solutions were prepared, one containing [NaOH (1.5 M) + Na_2CO_3 (0.5 M)] and the other containing $CdCl_3$ + VCl_3 (total metal concentration was 0.2 M), which was gradually added to the first solution with continuous stirring, and the pH was adjusted to 10 by the addition of NaOH. After complete precipitation, the temperature of the mixture was raised to 60°C with continuous stirring for 16 h. The mixture was cooled down to an ambient temperature. The precipitate was separated and washed several times with deionized water until pH 7. The product was separated by centrifugation (10 min, 500 min^{-1}).

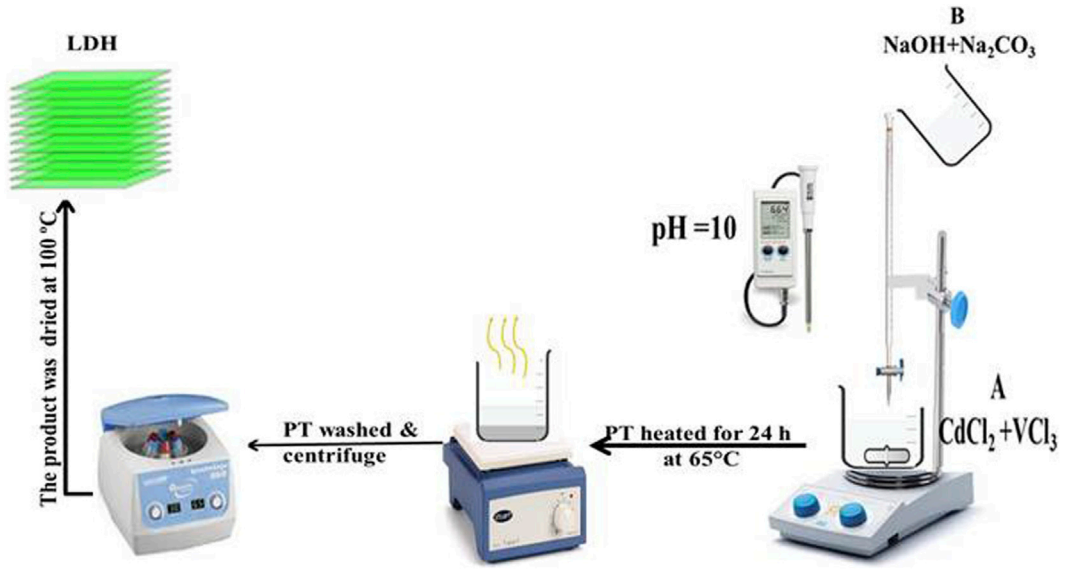

FIGURE 1
A schematic diagram of the synthesis process steps.

The LDH precipitate was dried at 100°C for 24 h and calcined at 300°C.

2.3 Characterization techniques

A Pan Analytical Model X′ Pert Pro system with Cu-K radiation (λ = 0.1542 nm) was used to record the XRD patterns. The nitrogen adsorption-desorption isotherms of the synthesized samples were recorded at −196°C on the Quantachrome NOVA automated gas sorption system. A JEOL JEM 3500 electron microscope was used for the (FE-SEM) examination. (FTIR) was recorded on the Nicolet is 50, Thermo Fisher Scientific FT-IR spectrophotometer. A JASCO-750 UV-Vis spectrometer has been used to measurement optical absorption. The VOLTALAB PGZ301 potentiostat was used for cyclic voltammetry and impedance studies. A photocell test and a visible light lamp with an intensity of 100 $mWcm^{-2}$ were used to measure the photocurrent density-voltage (J-V) output of the solar cell, which was calibrated using a radiometer (International Light Technologies 1700).

2.4 Fabrication of DSSCs (PA and PC)

ITO coated glass slides were cleaned and washed with ethanol, isopropanol, and deionized water in an ultrasonic bath for 20 min. The prepared Cd-V-LDH was mixed with X-100 and acetic acid to form a blend paste, and to get a stable photoanode, doctor blade printing was the most widely used coating technique for the preparation of DSSC layers due to its low cost, simple operation, and fewer moving parts. A paste of Cd-V-LDH is dropped on the substrate and spread using a sharp blade. Cd-V-LDH layer (4 cm^2) spread onto ITO was heated in a muffle furnace at 450°C for 10 min. After being cooled off to room temperature, the film was then dipped in a solution of EY for 24 h at ambient temperature. For the opposite electrode, GN, (GO), and (CC) were applied as PCs by depositing on the conducting side of ITO as in the same previous method. PA and PC electrodes were held together as a sandawitch, and the liquid electrolyte of (0.2 M LiI + 0.5I_2) in ethanol solution was completely absorbed into the electrodes by capillarity.

Different parameters affecting PCE were studied, e.g., EY concentration and pH, active area of PA, and types of PC. Different molar concentrations of EY were utilised for this purpose (3×10^{-3}, 1×10^{-3}, 5×10^{-4}, 3×10^{-4} and 5×10^{-5} M) and the Cd-V-LDH layer was doped in the EY bath for 24 h. Also, different pH of EY at 1.5, 3.5, 5.5, 9.5, and 13.5 were considered. Different types of PC were studied and applied, including GN, GO, and CC.

2.5 DSSCs output

In a solar box with photocell test equipment, the electrical characteristics of J-V curves were assessed. To determine PCE, the fill factor (FF) must first be determined using all cell outputs according to Eq. 1. It is simple to obtain the PCE by Eq after determining FF (Eq. 2).

$$FF = \frac{V_{pp} \times J_{pp}}{V_{oc} \times J_{sc}} \quad (1)$$

$$PCE\,\% = \frac{V_{oc} \times J_{sc} \times \mathrm{FF}}{I_s} \quad (2)$$

where Vpp and Jpp denote maximum power output voltage and current density, respectively. Whereas is the intensity of the incident light ($mW{\cdot}cm^{-2}$).

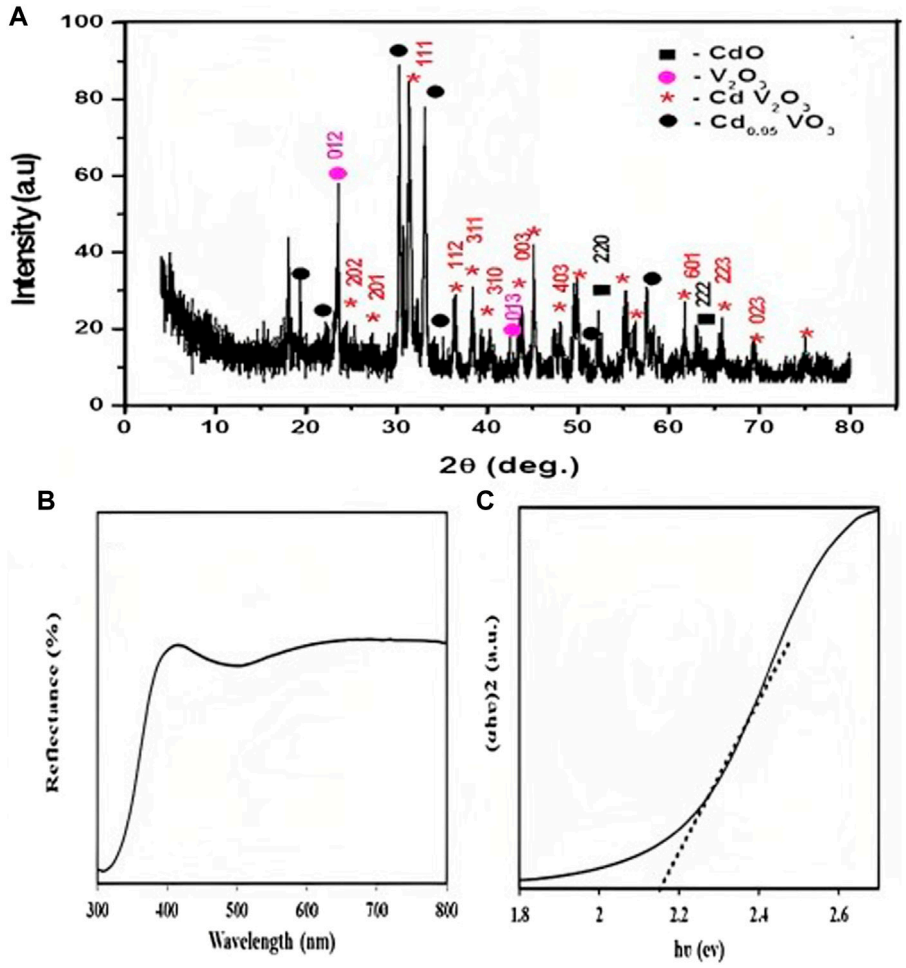

FIGURE 2
XRD **(A)**, diffuse reflectance **(B)**, and band-gap evaluation of the prepared **(C)**.

3 Results and discussion

3.1 Characteristic identification of PA

The XRD patterns of the synthesized sample are displayed in Figure 1. It shows that two phases of cadmium vanadium oxide are formed (Cd V_2O_3 and Cd $_{0.95}$ VO_3). The highest diffraction peaks at 2θ around 30.316° and 33.058° can be attributed to Cd $_{0.95}$ VO_3 phase, according to JCPDS card # 00-019-0195. Another diffraction peaks appear at 2θ values of 19.104°, 23.317°, 34.26°, 50.91°, and 57.53°. Peaks at 2θ values of 24.57°, 27.09°, 36.35°, 38.36°, 40.13°, 44.13°, 45.08°, 47.32°, 49.75°, 56.28°, 55.29°, 61.81°, 65.88°, 69.36°, and 74.85° correspond to Cd V_2O_3 (JCPDS card # 00-059-0581), while the main peak appears at 2θ value of 31.311°. There are two peaks at 2θ equal to 23.517° and 43.776° indicate the presence of vanadium oxide (V_2O_3) (JCPDS card-no-34-0187). Additional peaks at 2θ of 52.29° and 63.14° indicate the presence of cadmium oxide (CdO) according to JCPDS card # 01-104. The crystallite size (D) of PA was calculated using the Debye Scherrer Eq. 3.

$$D = \frac{k\lambda}{\beta COS\,\theta} \tag{3}$$

Where D is the crystallite size of nm, $k = 0.9$ is a correction factor that accounted for particle shapes, β is the full width at half maximum (FWHM) of the most intense diffraction peak plane, λ is the wavelength of the Cu target = 0.15406 nm, and θ is the Bragg angle, and the average crystallite size of the Cd-V- LDH was 16 nm.

Figure 2B shows diffuse reflectance (DRS) spectra and band gap determination. Figure 2B displays UV–Vis DRS graphs of the Cd-V-LDH and the data showed a strong peak in the visible range of 430 nm. Cd-V-LDH band gap energy can be calculated using Eq. 4 (Nayak and Parida, 2019).

$$(\alpha h\nu)^{1/n} = A(h\nu - Eg) \tag{4}$$

where α is the absorption coefficient, h is the Planck's constant, ν is the energy of incident light, A is an arbitrary constant, and Eg is the band gap energy of a material LDH. The nature of band gap transition depends upon the n value of a LDH material; $n = 1/2$ for direct transition and $n = 2$ for indirect transition. In this case, LDH is found to have direct transitions (Nayak and Parida, 2019). Therefore, the plot of (αhν)2 vs. hν (Kubelka–Munk function as a function of photon energy) gives the band gap energy value by extrapolating the straight line to the hν axis intercept (*X*-axis) as

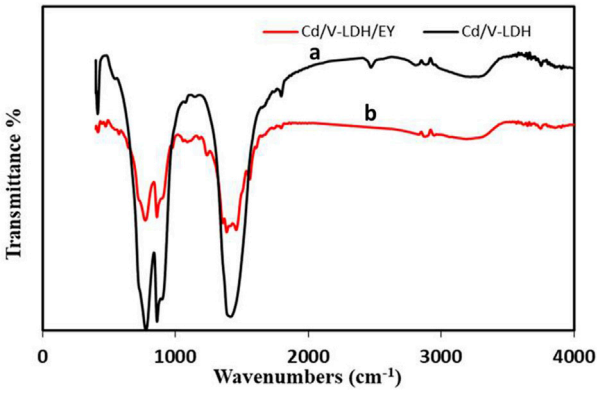

FIGURE 3
FTIR of Cd-V LDH (spectrum a) and Cd-V LDH after socking in EY dye (spectrum b).

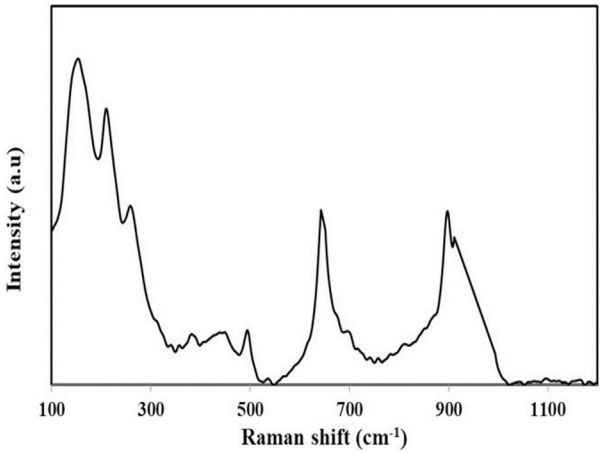

FIGURE 4
Raman spectrum of Cd-V LDH.

shown in Figure 2C. The estimated band gap energy value was found to be 2.1 eV. The band gap energy value of LDH exhibits a single band gap value, which is due to the strong coupling effect of constituent semiconductor components and simultaneous overlapping of band gap energies due to self-assembly of layered-to-layered structure. As a result, the band gap energy tuning of the as-fabricated heterostructure nanocomposite is due to the accessibility of quantum confinement effects, defect sites, or oxygen vacancies, which may increase the intensity of visible light absorption for superior photocatalytic activities (Zheng et al., 2019).

The FT-IR spectrum of Cd-V-LDH was displayed in Figure 3. The spectrum (a) shows bands at 3,421 and 1,637 cm^{-1} were associated with the interlayer water molecules in Cd-V-LDH (Wang et al., 2015). According to the literature (Kloprogge et al., 2002; Li et al., 2017), the strong band at 1,389 cm^{-1} was described as the carbonate anions' mode of v3 asymmetric stretching. α, β-unsaturated aliphatic esters appears from 1,730 to 1,715 cm^{-1}. All the vibration bands from 800 to 400 cm^{-1} were unique to the M-O, M-O-M, and O-M-O groups (Bazzan et al., 2011).

After immersing the Cd-V-LDH in EY at concentrations of 1 × 10^{-3} M for 24 h at pH 5.5, FTIR was used to categorise the adsorbed groups on the surface. The spectrum (b) shows the decrease in the intensity of the bands due to the implimination of these groups in the adsorption process (WangWang, 2008). Figure 3 shows also the formation of new functional groups on the surface of Cd-V-LDH after impregnation. The main bands were located in 1,097, 1,236, 1,355, 1,385, and 1,556 cm^{-1}. The presence of ether linkage C–O–C and C–O stretching was observed at 1,097 and 1,236 cm^{-1}. The band at 1,355, 1,385, and 1,556 cm^{-1} is assigned to acetate carboxyl groups (WangWang, 2008). From these results, we conclude that EY is attached to the Cd-V-LDH surface by carboxylate group.

Raman spectroscopic analysis was performed in this study to determine the nature of the bonding of the Cd-V-LDH Raman modes at 148, 207, 253, 324, 342, 374, 489, 520, 642, 895, 905, and 1,100 cm^{-1} are observed, as shown in Figure 4. The peaks between 100 and 314 cm^{-1}, which are associated with oxides of V modes, are primarily caused by the bending and lattice modes of V-O bonds. The peak at 320 cm^{-1} in the lower wavenumber area is connected with the motion of the cadmium sub-lattice and oxygen atoms in CdO, and it is associated with the second order scattering Raman mode ($E^2_{high} - E_{low}$) where E^2 is 2 non-polar. Due to imperfections such oxygen vacancies, the band with a wavelength of 374 cm^{-1} is first-order A1 (LO) mode (Samanta et al., 2006). Raman spectra's A1 or E1 modes show that the crystal lattice's or the sample's lattice vibrations are parallel to or perpendicular to the c-axis, respectively. Additionally, it is corroborated by the phonons' longitudinal and transverse optical emission. E1 (TO) may be to blame for the noticeable shift in peak position. These modes are indicative of the V position. Due to the stretching mode of (V2O2)n, which corresponds to chain translation, some Raman peaks are also seen at 148 cm^1 at lower frequencies (Boruah and Misra, 2016). The broad breadth of the peak at 255 cm^1 may be caused by the V-O-V bending mode (Julien et al., 1997). The stretching band and triply coordinated oxygen (V_3-O) bond may be responsible for the peak at 315 cm^1 (Wang et al., 2001).

The Raman mode at 253 cm^{-1} corresponds to both the Cd-O and V-O-Vbending mode. The vibrational modes with frequencies at 489 cm^{-1} indicate the presence of Cd-V-O symmetry and 526 cm^{-1} represents V-O-V stretching mode due to medium range force. The Raman modes at 905 correspond to the V_2O_5 phase and the lower intense peak at 1,100 indicate Cd-O.

895, 792, 693, 509, 460, 370, 204, and 142 cm^{-1} indicate the presence of the CdV_2O_6 phase, where the mode at 696 cm^{-1} is the strongest mode of CdV_2O_6 (Mounasamy et al., 2020). The Raman mode at 488 cm^{-1} is associated with Cd–V–O symmetry of the V_2O_5–CdO system.

FEG-SEM and textural analysis were carried out in Figure 5A, which shows hexagonal platelet-like morphology with a size of about 2 μm in width and about 78 nm in thickness.

The textural properties of the prepared Cd-V-LDH showed the adsorption–desorption isotherms of N_2 were carried out in Figures 5B, C. That will provide a deeper insight into the porosity and specific surface area of the samples. The isotherms were classified according to IUPAC as reversible type IV. This is a feature of materials that contain mesoporosity and have high adsorption energy. These often include hysteresis attributed to the

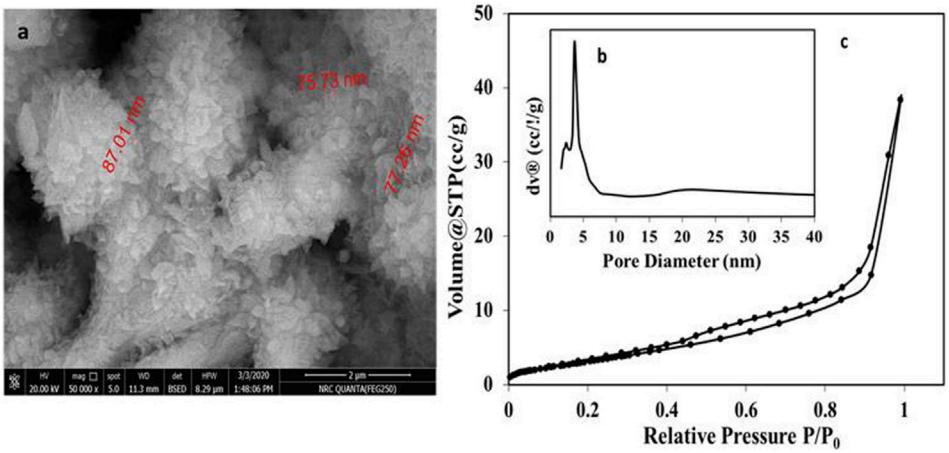

FIGURE 5
FE-SEM image **(A)**, pore size distribution **(B)**, and N2 adsorption-desorption isotherm of Cd-V LDH.

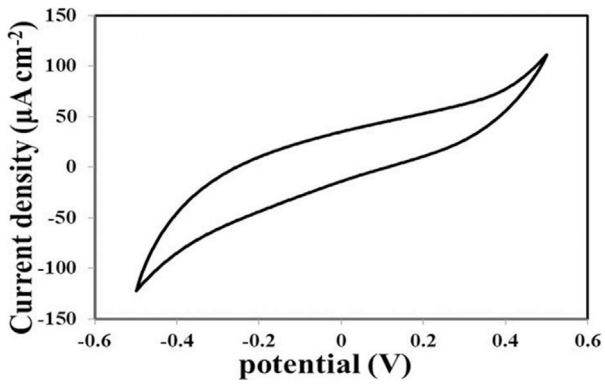

FIGURE 6
CV of Cd-V LDH.

mesoporosity, and the appearance of a hysteresis loop of H3-type indicates the presence of mesoporosity, and pores are represented by slit-shaped pore channels that are the result of the accumulation of plate-like layers. The pore diameters determined using the BJH method from the desorption curves of the isotherms was 3.66 nm, and the Brunauere Emmette Teller (BET) surface area was 22.65 m^2/g (Table 1).

Using cyclic voltammetric measurements, the electrochemical behaviour of the produced material was examined. The electrochemical experiments were conducted with (ITO) electrodes coated with Cd-V-LDH in 0.2 LiI M+0.5 M I2 as liquid electrolyte between 0.6 and −0.6 at a scan rate of 20 mVs^{-1}. No pairs of peaks that represent iodide (I) and triiodide (I_3^-) oxidation and reduction were observed in Figure 6, confirming optimal electric double-layer capacitance behaviours (Dang et al., 2016). The Cd-V-LDH electrode has a large integrated area under the curve due to better electron conduction and a higher degree of redox pseudocapacitance. The specific capacitance value calculated from the CV curve at 20 $mV{\cdot}s^{-1}$ is found to be 333.62 $F{\cdot}g^{-1}$.

3.2 DSSCs fabrication and investigation

After studying the constructed module system, J-V curves were obtained for (Cd-V-LDH/EY/LiI-I_2/GN system) under regular illumination of solar light, as shown in Figure 7. The cell's operation parameters are determined under various experimental conditions from the J-V curve characteristics., e.g., V_{OC}, J_{SC}, FF, and the overall PCE, which are calculated by Eqs.1, 2, respectively. Table 5 displays the cell's obtained parameters.

Photosensitization plays a significant role in the electrical output. Table 2 displays the electrical output at varied concentrations of EY. It was found that the cell sensitized with 1×10^{-3} M showed the highest electrical output, e.g., VOC (705 mV), JSC (12.40 mA/cm^2), and PCE (5.4%). Meanwhile, the cell utilizing at 5×10^{-5} M showed the lowest power generation; V_{OC} (330 mV), J_{SC} (8.88 mA/cm^2), and PCE (1.6%). This result agrees with the UV–Vis absorption spectrum.

The UV-vis of the samples with the highest and lowest concentrations of EY is shown in Figure 7A, EY absorbed the light primarily at 530 nm, and the absorption spectrum of the 1×10^{-3} M sample seems to be the highest one, so the most suitable concentration for EY to be adsorbed on the Cd-V-LDH surface was 1×10^{-3} M. EY was less effective in penetrating the LDH layer at higher concentrations. On the other side the amount of Photosensitizer atoms expected to absorb photons and provide an electron in the cell was limited at a low concentration, which results a drop in the output of the cell.

Furthermore, a shift in the pH of EY has the same effect as a shift in concentration. Table 3 indicates the influence of pH value on the cell's performance. The results indicated that the V_{OC} J_{SC}, FF and the overall PCE increase as the pH increases from 1.5 to 13.5 and the highest electrical output, i.e., V_{OC} of 705 mV, J_{SC} of 12.40 mA/cm^2 and PCE of 5.4%, was shown in an acidic medium at pH 5.5.

The electrical output was fall in strong acidic media (pH 1.5) due to fast degradation of EY, with resultant inefficient light harvesting by the dye (Isah et al., 2015). Additionally, if the pH drops, it is expected that probable acid leaching will degrade cell quality. While

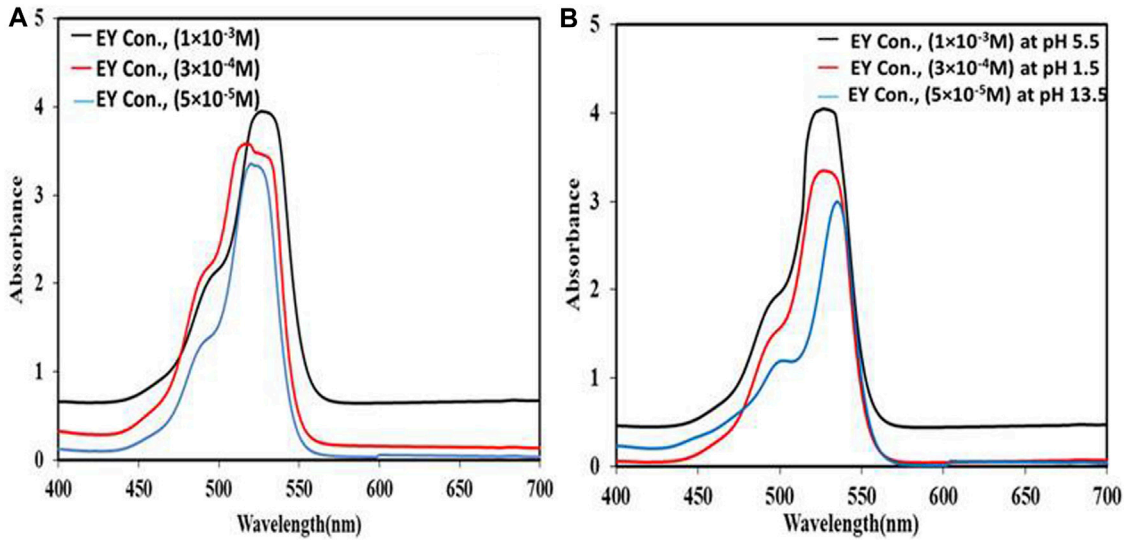

FIGURE 7
UV-vis absorption spectra of EY dye at different concentration **(A)** and different pH **(B)**.

TABLE 1 Surface area, pore volume and pore diameter characteristics of the prepared Cd-V-LDH.

Electrode	BET surface area, m^2/g	Pore volume, cc/g	Pore diameter, Å
Cd-V-LDH	22.65	0.063	3.66

TABLE 2 Performance of DSSC with different EY concentration, effect of EY concentration on Cd-V-LDH surface.

Dye conc. (M)	Voc (mV)	Jsc (mA cm^{-2})	FF	PCE%
3×10^{-3}	678	11.64	0.61	4.8
1×10^{-3}	705	12.40	0.62	5.4
3×10^{-4}	505	9.93	0.59	3.0
5×10^{-5}	330	8.88	0.56	1.6

pH 5.5, 0.2 LiI M + 0.5 M I_2, active area of WE 4.2 cm^2, GN as CE.

TABLE 3 Effect of pH of the dye on the performance of the cell.

pH	Voc (mV)	Jsc (mAcm^{-2})	FF	PCE%
1.5	673	11.69	0.61	4.8
5.5	705	12.40	0.62	5.4
9.5	624	10.51	0.58	3.8
13.5	558	10.03	0.56	3.1

EY conc., 1×10^{-3} M, 0.2 LiI M + 0.5 M I_2, active area of WE 4.2 cm^2, GN as CE.

in alkaline media at pH 13.5, the lowest electrical output was observed, i.e., V_{OC} of 558 mV, J_{SC} of 10.03 mA/cm^2 and PCE of 3.1%. This could be attributed to fall in optical absorbance of EY as shown in Figure 7B, as well as the negative charge can reduce possibility of the dye adsorption to the Cd-V-LDH surface.

The active area was defined as the effective area of PA that was exposed to visible light, with its value often ranging from 2 to 5 cm^2.

TABLE 4 Effect of active area of WE on the performance of the cell.

Active area (cm^2)	Voc (mV)	Jsc (mAcm^{-2})	FF	PCE%
2.6	530	10.5	0.43	2.4
3.4	610	12.1	0.46	3.3
4.2	705	12.4	0.62	5.4
4.8	430	8.53	0.38	1.5

EY conc., 1×10^{-3} M, pH 5.5, 0.2 LiI M + 0.5 M I_2, 0.06 M, GN as CE.

The effect of the active area on the cell's performance is seen in Table 4. Because PCE is directly impacted by FF, which is one of the cell's most important outputs, a DSSCS cell with high FF will also have high PCE. The internal resistance of the DSSCs had an impact on the FF. Therefore, the FF and PCE will be higher in an area that is more active.

A 4.2 cm^2 area yielded the highest PCE measurement. The FF reduced as the active area reached 5.8 cm^2, and the cause of this is attributed to the cell's rising internal resistance (Kang et al., 2003). The charge conveyance processes at GN as PC, the charge conveyance at the LDH/dye/electrolyte interface, permeation in the electrolyte, and the sheet resistance of ITO are all also related to the internal resistance (Han et al., 2005).

Cd-V-LDH has been applied as a photoanode, and the PCE increased to a maximum of 5.4% when the PA area was increased to 4.2 cm^2. The variation in PCE was shown in Table 4 as a function of PA size, and as the area rose to 4.8 cm^2, the PCE reduced by nearly 25%. Table 4 also showed that V_{OC}, J_{SC}, and FF varied depending on

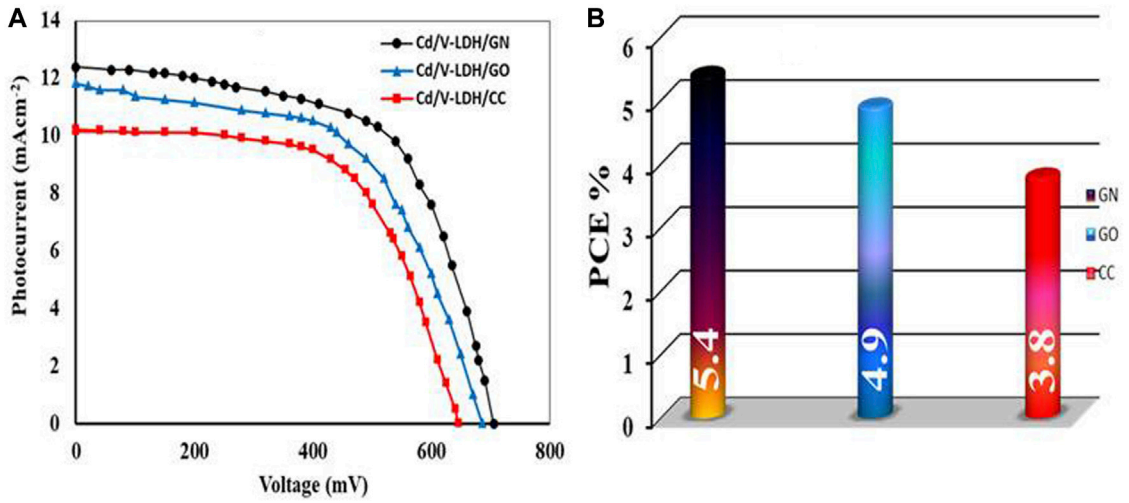

FIGURE 8
J-V curves of Cd-V with different CE **(A)** and the corresponding PCE of the cells **(B)**.

the active area. The equation below demonstrates how JSC followed a similar pattern to PCE and made a significant contribution to it. (Gregg and Hanna, 2003).

$$Jn(x) = n\mu(x)\nabla Fn \quad (6)$$

where n denotes the density of the electron and m(x) denotes its motion, and ∇Fn represents the gradient in the Fermi scale of the material's interface, and the reduction in J_{SC} indicates the loss of electrons for the ∇Fn and μ constants, meaning that as the area increases, the electrons' path length will be enlarged. Finally, recombination with the hole-conducting species in the electrolyte may result in an energy loss. As the area increases, VOC rates also decrease. At stable condition, the V_{OC} depends on the following factors: the electron density injected, the rate constant of the iodide reduction, and the conduction band electron density in the dark (Gregg and Hanna, 2003).

$$Voc - KT/e\ lnJ_{in}/ncbK_{rec}[I_3] \quad (7)$$

The PC has an important impact on the photovoltaic parameters of DSSCs. The PC undertakes some functions, e.g., as a catalyst, promotes the completion of mechanism operation, works as a positive electrode of primary cells; collects electrons from the external circuit and transmits them into the cell. So, the ultimate mission of the PC is to return the electrons from the external load back into the "circulation" inside the cell, and as a mirror, it reflects the unabsorbed light from the cell back into the cell to promote utilization of sunlight (Wu et al., 2017). Figure 8 depicts the J–V curves of DSSCs prepared by Cd-V-LDH as PA with different types of PC, i.e., GN, GO, and CC.

Table 5 displays the photovoltaic parameters from J–V curves and a brief comparison with other PCs. According to the data, the GN-based cell had a PCE of 5.4%, which is higher than the GO and CC electrodes. The PC activity affects on the cell's PCE, which synergizes the reduction reaction at the electrolyte/PC interface, which in turn support the restoration of the ground state of the

TABLE 5 Effect of CE on the performance of the cell.

LDH Sample	Voc, (mV)	Jsc, (mAcm^{-2})	FF	PCE%
Cd-V-LDH/GN	705	12.40	0.62	5.4
Cd-V-LDH/GO	683	11.91	0.61	4.9
Cd-V-LDH/CC	645	10.22	0.59	3.8

EY conc., 1 × 10^{-3} M, pH 5.50.2 LiI M + 0.5 M I_2, 0.06 M, active area of WE 4.2 cm^2.

organometallic EY at the electrolyte/photoanode interface. GN can be thought of as a layered material similar to graphene with nitrogen substituted. GN has superior qualities to graphene due to the presence of nitrogen atoms, a strong electronegativity, and a triazine-rich structure (Fu et al., 2014). Additionally, GN exhibits high electrocatalytically active sites, which increases its capability for the I_3^- reduction reaction. (Afshari et al., 2018). Finally, GN can retard backward transportation of electrons between PA and photosensitizer (Fan et al., 2017).

As shown in Table 5, the highest parameters for the fabricated cell were V_{OC} (705 mV),J_{SC} (12.40 mA/cm^2), FF (0.62), and PCE(5.4%) for Cd-V/EY-GN compared with results for [Cd-V/EY-GO] VOC (683 mV), J_{SC} (11.91 mA/cm^2), FF (0.61), and PCE (4.9%) and [Cd-V/EY-CC] VOC (645 mV), J_{SC} (10.22 mA/cm^2), FF (0.59), and PCE (3.8%), respectively.

3.3 Stability tests of Cd-V-LDH/GN system

With an active area of 4.2 cm^2, 0.2 LiI M + 0.5 M I_2 as liquid electrolyte, and GN as PC, a long-term stability test for Cd-V-LDH was conducted at light intensity of 100 mW/cm^2. The results revealed that the DSSCs were stable for 10 days under usual conditions.

Figure 9 shows the values for V_{OC}, J_{SC}, FF, and PCE as they changed over time. The starting parameters for (V_{OC}, J_{SC}, FF, and

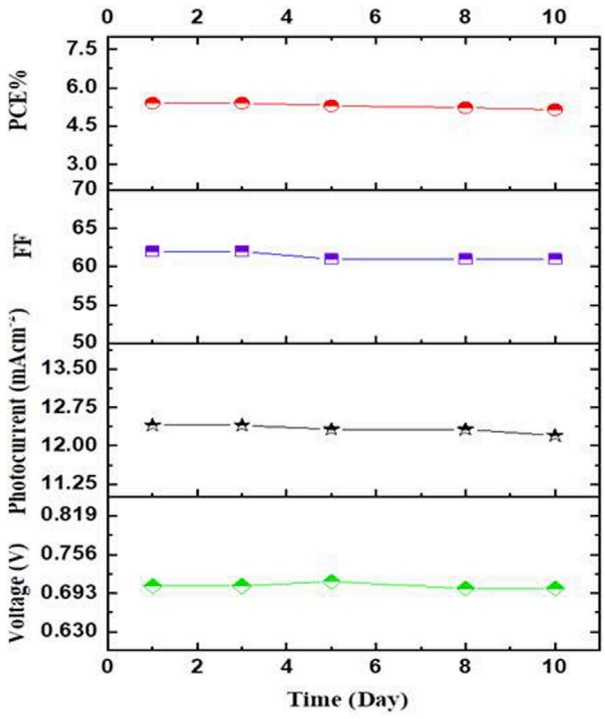

FIGURE 9
Stability of Cd-V-LDH/GN system.

PCE) are 705 mV, 12.40 mAcm^{-2}, 0.62, and 5.4%, respectively. All parameters were steady for the first 3 days of the test period. VOC varied between a slight increase during the course of the following 3 days to reach 712 mV and a slight decline by the end of the test to reach 701 mV, which only drops by 4 mV from the initial value (705 mV), demonstrating high adsorption stability of the Cd-V-LDH/GN system. J_{SC} showed a slight decline to 12.25 mAcm^{-2} and eventually reached 12.16 mAcm^{-2} at the conclusion of the test (10 days), this may be due to slow EY deterioration. After absorbing visible light for 10 days, the PCE gradually deteriorated to 5.15% and the system stayed at 95% of its initial value. The high cell stability demonstrated that the EY was very stable on the surface of Cd-V-LDH and that the degradation was limited.

4 Conclusion

In summary, a new material of layer double hydroxide (Cd-V-LDH) was prepared through an economical and simple coprecipitation method. The divalent M2+ cations (Cd^{2+}) and trivalent (V^{3+}) were taken in a 1:1 M ratio. The XRD and SEM analyses verified that LDH was formed. This is also supported by FTIR analysis, and UV spectroscopy was used to characterise the optical properties. The bandgap was determined from UV absorption and higher photocatalytic data existed in the visible region, and the electro catalytic activity was explained by EIS and CV. Series DSSCs from Cd-V-LDH and GN as PA and PC were discussed with other different parameters, e.g., impact of EY (concentration and pH), impact of active area of PA, and impact of PC type. The results show that the prepared Cd-V-LDH has been successful as a PA in DSSCs, which have a small particle size which will improve the dye-loading capability and facilitate the charge separation of the photogenerated charge carriers, therefore the Cd-V-LDH/GN system's achieved the best PCE at 5.4%. GN was also applied as PC enhanced the photocurrent and decreased the internal resistance of the DSSCs to extend the lifetime of electrons. Thus, the DSSCs based on Cd-V-LDH/GN reached a higher PCE (5.4%) compared with Cd-V-LDH/GO and Cd-V-LDH/CC PCE of 4.9% and 3.8%, respectively. That returns to the slow electron transport and the high charge recombination in the photoanode.

Data availability statement

The original contributions presented in the study are included in the article/Supplementary Material, further inquiries can be directed to the corresponding author.

Author contributions

SB: conceptualization, methodology, data collection, analysis, investigation, and writing-draft. AH: methodology, analysis, investigation, and writing-draft. SM: conceptualization, methodology, investigation, writing-original draft, and writing-reviewing and editing. All authors contributed to the article and approved the submitted version.

Conflict of interest

The authors declare that the research was conducted in the absence of any commercial or financial relationships that could be construed as a potential conflict of interest.

Publisher's note

All claims expressed in this article are solely those of the authors and do not necessarily represent those of their affiliated organizations, or those of the publisher, the editors and the reviewers. Any product that may be evaluated in this article, or claim that may be made by its manufacturer, is not guaranteed or endorsed by the publisher.

References

Abd-Ellatif, W. R., Mahmoud, N. G., Hashem, A. A., El-Aiashy, M. K., Ezzo, E. M., and Mahmoud, S. A. (2022). Efficient photodegradation of E124 dye using two-dimensional Zn-Co LDH: kinetic and thermodynamic studies. *Environ. Technol. Innov.* 27, 102393. doi:10.1016/j.eti.2022.102393

Afshari, M., Dinari, M., and Momeni, M. M. (2018). Ultrasonic irradiation preparation of graphitic-C3N4/polyaniline nanocomposites as counter electrodes for dye-sensitized solar cells. *Ultrason. Sonochemistry* 42, 631–639. doi:10.1016/j.ultsonch.2017.12.023

Andrea, F., Sangiorgi, N., Tosi Brandi, E., Sangiorgi, A., Mariani, F., Scavetta, E., et al. (2021). Increased efficiency and stability of Dye-Sensitized Solar Cells (DSSC) photoanode by intercalation of Eosin Y into Zn/Al layered double hydroxide. *Appl. Clay Sci.* 212, 106219. doi:10.1016/j.clay.2021.106219

Bazzan, G., Deneault, J. R., Kang, T. S., Taylor, B. E., and Durstock, Mi.F. (2011). Nanoparticle/dye interface optimization in dye-sensitized solar cells. *Adv. Funct. Mater.* 21, 3268–3274. doi:10.1002/adfm.201100595

Benito, P., Guinea, I., Herrero, M., Labajos, M. F., and Rives, V. (2007). Incidence of microwave hydrothermal treatments on the crystallinity properties of hydrotalcite-like compounds. *Z. Anorg. Allg. Chem.* 633, 1815–1819. doi:10.1002/zaac.200700178

Boruah, B. D., and Misra, A. (2016). Energy-efficient hydrogenated zinc oxide nanoflakes for high-performance self-powered ultraviolet photodetector. *ACS Appl. Mater Interfaces* 8, 18182–18188. doi:10.1021/acsami.6b04954

Cao, J., Zhao, Y., Zhu, Y., Yang, X., Shi, P., Xiao, H., et al. (2017a). Preparation and photovoltaic properties of CdS quantum dot-sensitized solar cell based on zinc tin mixed metal oxides. *J. Colloid Interface Sci.* 498, 223–228. doi:10.1016/j.jcis.2017.03.061

Cao, J., Zhu, Y., Yang, X., Chen, Y., Li, Y., Xiao, H., et al. (2016). The promising photo anode of graphene/zinc titanium mixed metal oxides for the CdS quantum dot-sensitized solar cell. *Sol. Energy Mater. Sol. Cells* 157, 814–819. doi:10.1016/j.solmat.2016.08.003

Cao, J., Zhu, Y., Yang, X., Liu, S., Liu, D., Tang, X., et al. (2017b). Graphene/zinc aluminum mixed metal oxides photo anode for CdS quantum dot-sensitized solar cell. *Mater. Res. Express* 4, 045501. doi:10.1088/2053-1591/aa6774

Caschera, D., Federici, F., Zane, D., Focanti, F., Curulli, A., and Padeletti, G. (2009). Gold nanoparticles modified GC electrodes: electrochemical behaviour dependence of different neurotransmitters and molecules of biological interest on the particles size and shape. *J. Nanoparticle Res.* 11, 1925–1936. doi:10.1007/s11051-008-9547-0

Dang, Y. Q., Ren, S. Z., Liu, G., Cai, J., Zhang, Y., and Qiu, J. (2016). Electrochemical and capacitive properties of carbon dots/reduced graphene oxide supercapacitors. *Nanomaterials* 6, 212. doi:10.3390/nano6110212

Fan, K., Yu, J., and Ho, W. (2017). Improving photoanodes to obtain highly efficient dye-sensitized solar cells: a brief review. *Mater. Horiz.* 4, 319–344. doi:10.1039/c6mh00511j

Foruzin, L. J., Rezvani, Z., and Nejati, K. (2016). Fabrication of TiO2@ZnAl-layered double hydroxide based anode material for dye-sensitized solar cell. *RSC Adv.* 6, 10912–10918. doi:10.1039/c5ra23384d

Foruzin, L. J., Zolfaghar, R., and Kamellia, N. (2019). TiO2@ NiAl-Layered double oxide nanocomposite: an excellent photoanode for a dye sensitized solar cell. *Sol. Energy* 186, 106–112. doi:10.1016/j.solener.2019.05.005

Fu, Y., Zhu, J., Hu, C., Wu, X., and Wang, X. (2014). Covalently coupled hybrid of graphitic carbon nitride with reduced graphene oxide as a superior performance lithium-ion battery anode. *Nanoscale* 6, 12555–12564. doi:10.1039/c4nr03145h

Ge, Z., Wang, C., Chen, T., Chen, Z., Wang, T., Guo, L., et al. (2021). Preparation of Cu-doped ZnO nanoparticles via layered double hydroxide and application for dye-sensitized solar cells. *J. Phys. Chem. Solids* 150, 109833. doi:10.1016/j.jpcs.2020.109833

Grätzel, M. (2003). Dye-sensitized solar cells. *J. Photochem. Photobiol. C Photochem. Rev.* 4, 145–153. doi:10.1016/s1389-5567(03)00026-1

Gregg, B. A., and Hanna, M. C. (2003). Comparing organic to inorganic photovoltaic cells: theory, experiment, and simulation. *J. Appl. Phys.* 93, 3605–3614. doi:10.1063/1.1544413

Hagfeldt, A., Boschloo, G., Sun, L., Kloo, L., and Pettersson, H. (2010). Dye-sensitized solar cells. *Chem. Rev.* 110, 6595–6663. doi:10.1021/cr900356p

Han, L., Koide, N., Chiba, Y., Islam, A., Komiya, R., Fuke, N., et al. (2005). Improvement of efficiency of dye-sensitized solar cells by reduction of internal resistance. *Appl. Phys. Lett.* 86, 213501. doi:10.1063/1.1925773

Isah, K. U., Ahmadu, U., Idris, A., Kimpa, M. I., Uno, U. E., Ndamitso, M. M., et al. (2015). Betalain pigments as natural photosensitizers for dye-sensitized solar cells: the effect of dye pH on the photoelectric parameters. *Mater. Renew. Sustain. Energy* 4, 86–93. doi:10.56431/p-nw0514

Julien, C., Nazri, G. A., and Bergstrom, O. (1997). Raman scattering studies of microcrystalline V6O13. *Basic Solid State Phys.* 201, 319–326. doi:10.1002/1521-3951(199705)201:1<319:aid-pssb319>3.0.co;2-t

Kang, M. G., Park, N. G., Park, Y. J., Ryu, K. S., and Chang, S. (2003). Manufacturing method for transparent electric windows using dye-sensitized TiO2 solar cells. *Sol. Energy Material Sol. Cells* 75, 475–479. doi:10.1016/s0927-0248(02)00202-7

Ke, D., Peng, T., Ma, L., Cai, P., and Dai, K. (2009). Effects of hydrothermal temperature on the microstructures of BiVO4 and its photocatalytic O2 evolution activity under visible light. *Inorg. Chem.* 48, 4685–4691. doi:10.1021/ic900064m

Kloprogge, J. T., Wharton, D., Hickey, L., and Frost, R. L. (2002). Infrared and Raman study of interlayer anions CO_3^{2-}, NO3–, SO_4^{2-} and ClO^{4-} in Mg/Al-hydrotalcite. *Am. Mineralogist* 87, 623–629. doi:10.2138/am-2002-5-604

Kohtani, S., Koshiko, M., Kudo, A., Tokumura, K., Ishigaki, Y., Toriba, A., et al. (2003). Photodegradation of 4-alkylphenols using BiVO4 photocatalyst under irradiation with visible light from a solar simulator. *Appl. Catal. B* 46, 573–586. doi:10.1016/s0926-3373(03)00320-5

Li, J., Zhang, S., Chen, Y., Liu, T., Liu, C., Zhang, X., et al. (2017). A novel three-dimensional hierarchical CuAl layered double hydroxide with excellent catalytic activity for degradation of methyl orange. *RSC Adv.* 7, 29051–29057. doi:10.1039/c7ra03848h

Li, J. S., Zhang, D. Q., and Yu, J. C. (2008). Ordered mesoporous BiVO4 through nanocasting: a superior visible light-driven photocatalyst. *Chem. Mater.* 20, 3983–3992. doi:10.1021/cm800236z

Mahmoud, S. A., Emam, M., and Hegazy, W. (2021b). Assessment of hydrogen sulfide gas in petroleum company and photocatalytic degradation using mesoporous TiO2 nanostructured thin films. *Egypt. J. Chem.* 64, 5919–5927. doi:10.21608/EJCHEM.2021.68185.3486

Mahmoud, S. A., Atia, H., and Bendary, S. H. (2016). Synthesis of a high efficiency novel working electrode scandium/HOMBIKAT in dye-sensitized solar cells. *Sol. Energy* 134, 452–460. doi:10.1016/j.solener.2016.05.022

Mahmoud, S. A., Bendary, S. H., Atia, H., and Martin, A. (2017). Effect of different electrolytes on the efficiency of dye sensitized solar cells for solar energy conversion. *J. Nanosci. Nanotechnol.* 17, 3719–3728. doi:10.1166/jnn.2017.14004

Mahmoud, S. A., Bendary, S. H., Salem, A. A., and Osama, A. F. (2019). Facile synthesis of high yield two-dimensional zinc vanadate nanoflakes. *SN Appl. Sci.* 1, 497. doi:10.1007/s42452-019-0508-2

Mahmoud, S. A., Elsisi, M. E., and Mansour, A. F. (2022). Synthesis and electrochemical performance of α-Al2O3 and M-Al2O4 spinel nanocomposites in hybrid quantum dot-sensitized solar cells. *Sci. Rep.* 12, 17009. doi:10.1038/s41598-022-21186-4

Mahmoud, S. A., Fouad, O. A., Salem, A. A., and Bendary, S. H. (2021a). Profound impact of Zn3 (OH) 2 (V2O7)(H2O) 2 and Zn3V2O8–Zn2V2O7 in dye sensitized solar cells. *J. Electron. Mater.* 50 (8), 4289–4302. doi:10.1007/s11664-021-08860-5

Mahmoud, S. A., and Fouad, O. A. (2015). Synthesis and application of zinc/tin oxide nanostructures in photocatalysis and dye sensitized solar cells. *Sol. Energy Mater. Sol. Cells* 136, 38–43. doi:10.1016/j.solmat.2014.12.035

Mitchell, S., Biswick, T., Jones, W., Williams, G., and O'Hare, D. (2007). A synchrotron radiation study of the hydrothermal synthesis of layered double hydroxides from MgO and Al2O3 slurries. *Green Chem.* 9, 373–378. doi:10.1039/b613795d

Mostafa, M. S., and Mohamed, N. H. (2016). Towards novel adsorptive nanomaterials: synthesis of $Co^{2+}Mo^{6+}$ LDH for sulfur and aromatic removal from crude petrolatum. *Egypt. J. Petroleum* 25, 221–227. doi:10.1016/j.ejpe.2015.05.013

Mounasamy, V., Mani, G. K., Ponnusamy, D., Tsuchiya, K., Reshma, P. R., Prasad, A. K., et al. (2020). Cadmium metavanadate mixed oxide nanorods for the chemiresistive detection of methane molecules. *New J. Chem.* 44, 12473–12485. doi:10.1039/d0nj02690e

Nayak, S., and Parida, K. M. (2019). Deciphering Z-scheme charge transfer dynamics in heterostructure NiFe-LDH/N-rGO/g-C3N4 nanocomposite for photocatalytic pollutant removal and water splitting reactions. *Sci. Rep.* 9, 2458. doi:10.1038/s41598-019-39009-4

O'regan, B., and Grätzel, M. (1991). A low-cost, high-efficiency solar cell based on dye-sensitized colloidal TiO2 films. *Nature* 353, 737–740. doi:10.1038/353737a0

Oshikiri, M., Boero, M., Ye, J., Zou, Z., and Kido, G. (2002). Electronic structures of promising photocatalysts InMO4 (M=V, Nb, Ta) and BiVO4 for water decomposition in the visible wavelength region. *Chem. Phys.* 117, 7313–7318. doi:10.1063/1.1507101

Samanta, K., Bhattacharya, P., Katiyar, R. S., Iwamoto, W., Pagliuso, P. G., and Rettori, C. (2006). Raman scattering studies in dilute magnetic semiconductor Zn1−xCoxO. *Phys. Rev. B* 73, 245213–245215. doi:10.1103/PhysRevB.73.245213

Sayama, K., Nomura, A., Zou, Z. G., Abe, R., Abe, Y., and Arakawa, H. (2003). Photoelectrochemical decomposition of water on nanocrystalline $BiVO_4$ film electrodes under visible light. *Chem. Commun.*, 2908–2909. doi:10.1039/b310428a

Shiba, K., and Ogawa, M. (2018). Precise Synthesis of well-defined inorganic-organic hybrid particles. *Chem. Rec.* 18, 950–968. doi:10.1002/tcr.201700077

Tonelli, D., Isacco, G., Elisa, M., and Scavetta, E. (2021). Synthesis and characterization of layered double hydroxides as materials for electrocatalytic applications. *Nanomater. (Basel).* 11, 725. doi:10.3390/nano11030725

Walsh, A., Yan, Y. F., Huda, M. N., Al-Jassim, M. M., and Wei, S. H. (2009). Band edge electronic structure of BiVO4: elucidating the role of the Bi s and V d orbitals. *Chem. Mater.* 21, 547–551. doi:10.1021/cm802894z

Wang, C., Zhu, Y., Ge, Z., Shi, R., Chen, T., Chen, Z., et al. (2020). The feasible photoanode of graphene oxide/zinc aluminum mixed metal oxides for the dye-sensitized solar cell. *Colloid Interface Sci. Commun.* 39, 100313. doi:10.1016/j.colcom.2020.100313

Wang, X. J., Li, H. D., Fei, Y. J., Weng, X., Xiong, Y. Y., Nie, Y. X., et al. (2001). XRD and Raman study of vanadium oxide thin films deposited on fused silica substrates by RF magnetron sputtering. *Appl. Surf. Sci.* 177, 8–14. doi:10.1016/s0169-4332(00)00918-1

Wang, X., Spörer, Y., Leuteritz, A., Kuehnert, I., Wagenknecht, U., Heinrich, G., et al. (2015). Comparative study of the synergistic effect of binary and ternary LDH with

intumescent flame retardant on the properties of polypropylene composites. *RSC Adv.* 5, 78979–78985. doi:10.1039/c5ra15565g

WangWang, LiAiqin (2008). Adsorption properties of Congo red from aqueous solution onto N,O-carboxymethyl-chitosan. *Bioresour. Technol.* 99, 1403–1408. doi:10.1016/j.biortech.2007.01.063

Wu, J., Lan, Z., Lin, J., Huang, M., Huang, Y., Fan, L., et al. (2017). Counter electrodes in dye-sensitized solar cells. *Chem. Soc. Rev.* 46, 5975–6023. doi:10.1039/c6cs00752j

Xu, F., and Sun, L. (2011). Solution-derived ZnO nanostructures for photoanodes of dye-sensitized solar cells. *Energy and Environ. Sci.* 4, 818–841. doi:10.1039/c0ee00448k

Xu, P. Z., and Lu, Q. G. (2005). Hydrothermal synthesis of layered double hydroxides (LDHs) from mixed MgO and Al_2O_3: LDH formation mechanism. *Chem. Mater.* 17, 1055–1062. doi:10.1021/cm048085g

Ye, J., Zou, Z., Oshikiri, M., Matsushita, A., Shimoda, M., Imai, M., et al. (2002). A novel hydrogen-evolving photocatalyst InVO4 active under visible light irradiation. *Chem. Phys. Lett.* 356, 221–226. doi:10.1016/s0009-2614(02)00254-3

Zhang, L., Liu, J., Xiao, H., Liu, D., Qin, Y., Wu, H., et al. (2014). Preparation and properties of mixed metal oxides based layered double hydroxide as anode materials for dye-sensitized solar cell. *Chem. Eng. J.* 250, 1–5. doi:10.1016/j.cej.2014.03.098

Zhang, P., and Dai, S. (2017). Mechanochemical synthesis of porous organic materials. *J. Mater. Chem. A* 5, 16118–16127. doi:10.1039/c7ta04829g

Zhao, Y., Li, F., Zhang, R., Evans, D. G., and Duan, X. (2002). Preparation of layered double-hydroxide nanomaterials with a uniform crystallite size using a new method involving separate nucleation and aging steps. *Chem. Mater.* 14, 4286–4291. doi:10.1021/cm020370h

Zhao, Y., Xie, Y., Zhu, X., Yan, S., and Wang, S. X. (2008). Surfactant-free synthesis of hyperbranched monoclinic bismuth vanadate and its applications in photocatalysis, gas sensing, and lithium-ion batteries. *Chem. Eur. J.* 14, 1601–1606. doi:10.1002/chem.200701053

Zheng, Y., Cheng, B., You, W., Yu, J., and Ho, W. (2019). 3D hierarchical graphene oxide-NiFe LDH composite with enhanced adsorption affinity to Congo red, methyl orange and Cr (VI) ions. *J. Hazard. Mater.* 369, 214–225. doi:10.1016/j.jhazmat.2019.02.013

Zhu, Y., Wang, D., Yang, X., Liu, S., Liu, D., Liu, J., et al. (2017a). Investigation of the dye-sensitized solar cell designed by a series of mixed metal oxides based on ZnAl-layered double hydroxide. *Appl. Phys. A* 123, 641–648. doi:10.1007/s00339-017-1256-z

Zhu, Y., Wang, D., Yang, X., Liu, S., Liu, D., Liu, J., et al. (2017b). Investigation of the dye-sensitized solar cell designed by a series of mixed metal oxides based on ZnAl-layered double hydroxide. *Phys. A* 123, 641. doi:10.1007/s00339-017-1256-z

Zou, Z., Ye, J., Sayama, K., and Arakawa, H. (2001). Photocatalytic and photophysical properties of a novel series of solid photocatalysts, Bi2MNbO7 (M = Al^{3+}; Ga^{3+} and In^{3+}). *Chem. Phys. Lett.* 333, 57–62. doi:10.1016/s0009-2614(00)01348-8